

# Saturable absorption in diamond nanophotonics

Christopher Coutts,<sup>1,4,\*</sup> Nicholas J. Sorensen,<sup>1,4</sup> Elham Zohari,<sup>1,2,3</sup> Sean McNaney,<sup>1</sup>  
Sigurd Flågan,<sup>1</sup> and Paul E. Barclay<sup>1</sup>

<sup>1</sup> *Institute for Quantum Science and Technology, University of Calgary, Calgary, AB, T2N 1N4, Canada*

<sup>2</sup> *Department of Physics, University of Alberta, Edmonton, Alberta, T6G 2R3, Canada*

<sup>3</sup> *National Research Council of Canada, Quantum and Nanotechnology Research Centre, Edmonton, Alberta, T6G 2M9, Canada*

<sup>4</sup> *The authors contributed equally to this work.*

\**christopher.coutts@ucalgary.ca*

## Abstract

Diamond is a leading quantum photonics platform due to its ability to host qubits based on crystal defects such as nitrogen vacancy centres. Fabricating nanophotonic devices from defect-rich diamond, which is central to many quantum sensing technologies, promises to enable enhanced performance and integrability of diamond quantum sensors. Here we demonstrate microdisk cavities fabricated from defect-rich diamond that support optical modes with high quality factor ( $Q \sim 7 \times 10^4$  at 1042 nm), and show that they exhibit saturable absorption. Power dependent spectroscopy measurements spanning 979 nm to 1604 nm are used to extract wavelength-dependent absorption coefficients and saturation intensities, which indicate that a hydrogen-related defect is a likely origin of the observed absorption. At 1047 nm, we measure a saturation intensity of 3.3 (1) MW/cm<sup>2</sup> and an absorption coefficient of 0.537 (5) cm<sup>-1</sup>. These results provide insight into defect-mediated optical loss in diamond nanophotonics and suggest strategies to harness defect-induced nonlinearities in future diamond photonic devices.

## 1 Introduction

Diamond holds tremendous promise for quantum photonic technologies due to its wide electronic bandgap, its exceptional thermal properties, and its ability to host optically addressable defects that function as spin qubits [1]. In addition, diamond cavities can strongly confine light and operate at extreme optical intensities without sustaining optical damage [2, 3]. Such operating regimes significantly enhance light-matter interactions and, together with advances in fabrication techniques [4–7], have enabled diamond nanophotonic cavities for applications including nonlinear optics [3, 8–10], cavity-enhanced spin-photon interactions [11–13], and optomechanics [6, 14, 15]. Realizing cavities fabricated from material engineered to host dense ensembles of defects is of growing interest for quantum technologies [16]; however, the impact of such defects on the optical properties of nanophotonic devices has not been studied.

As illustrated in Fig. 1, optical cavities resonantly circulate light and enhance light-matter interactions [17]. The performance of optical cavities in many applications can be characterized by the ratio of cavity quality factor to effective mode volume,  $Q/V$ , and is inversely proportional to the energy loss rate of the cavity,  $Q \propto 1/\kappa$  (see Appendix A). Cavity loss arises from several mechanisms that contribute to distinct loss rates: the intrinsic loss rate  $\kappa_i$ , the external loss rate  $\kappa_{\text{ex}}$ , the parasitic loss rate  $\kappa_p$ , and the absorption loss rate  $\kappa_a$ . Coupling to radiation

modes due to fundamental leakage, as well as scattering from fabrication-induced imperfections and surface roughness, contributes to  $\kappa_i$ . Coupling to the output and leaky modes of a waveguide used to input and collect light from the cavity is captured by  $\kappa_{\text{ex}}$  and  $\kappa_p$ , respectively, while optical absorption by defects contributes to  $\kappa_a$ .

At low optical intensities ( $I$ ), these loss rates are typically assumed to be power-independent. However, absorption can exhibit nonlinear behaviour at high  $I$ , leading to an intensity-dependent internal loss rate for the cavity,  $\kappa_c$ :

$$\kappa_c(I) = \kappa_i + \kappa_p + \kappa_a(I). \quad (1)$$

In previous studies of diamond nanophotonic devices, defect-related absorption has not been reported, in part because devices are typically fabricated from high [6] or ultrahigh [14] purity material. However, diamond quantum sensing applications often benefit from samples with high defect density [18, 19]. Of the many optically active defects in diamond [20], including nitrogen- [21], hydrogen- [22], and group-IV-based [11, 23, 24] aggregates (see Fig. 1 (b)), spin-defects like the nitrogen-vacancy (NV) and the silicon-vacancy have been extensively studied for quantum networking [11, 12, 25–27] and sensing [28, 29] applications. Furthermore, samples engineered to support high spin-defect densities often host additional undesired defects like the nitrogen-vacancy-nitrogen (N<sub>2</sub>V) [30] and nitrogen-vacancy-hydrogen [31].

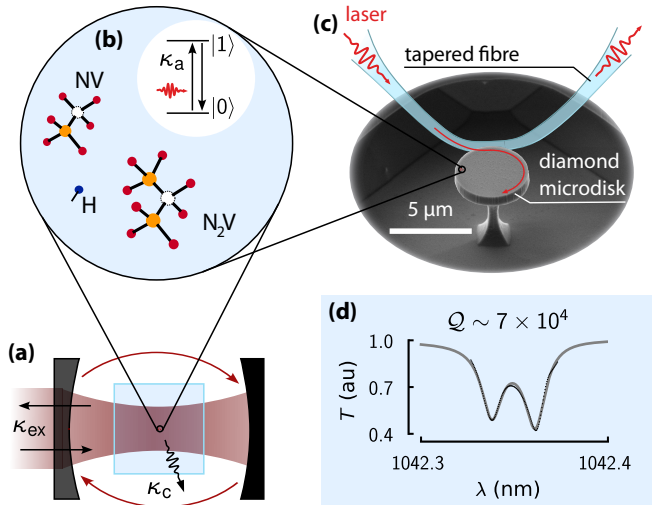


**Figure 1 – Loss in a diamond cavity.** (a) A diamond crystal inside a Fabry-Perot cavity. Photons are side-coupled into the cavity at rate  $\kappa_{\text{ex}}$ , whose linewidth is determined by the total optical cavity loss,  $\kappa = \kappa_{\text{ex}} + \kappa_c$ . Various mechanisms contribute to the cavity loss rate  $\kappa_c$ , and in highly doped samples absorption loss from defects is significant. (b) The diamond crystal hosts a variety of different point defects, several of which cause absorption loss ( $\kappa_a$ ) including hydrogen-based defects (H), and nitrogen-based defects like the NV centre and the  $\text{N}_2\text{V}$  centre. (c) A scanning electron micrograph reveals the diamond microdisk used to study the absorption dynamics. A fibre-taper waveguide is used to couple light into the microdisk, and changes in the transmission spectrum are used to characterize saturable absorption by the whispering-gallery mode (d). Fitting the transmission spectrum of the mode at 1042.35 nm, we find quality factors of  $Q_s = 71.6(6) \times 10^3$  and  $Q_a = 76.0(5) \times 10^3$  for the two dips corresponding to the symmetric and anti-symmetric standing wave modes of the WGM, respectively.

Because high- $Q/V$  cavities create large intracavity intensities for modest input powers and exhibit an optical response that is affected by small changes in  $\kappa_c$ , they can reveal nonlinear optical processes related to these defects that are not easily observable in bulk samples.

In this work, we realize microdisk cavities fabricated from dense-NV “quantum-grade” diamond ( $[\text{NV}] \sim 4.5 \text{ ppm}$  [19]), an example of which is shown in Fig. 1 (c). These devices support optical whispering-gallery modes (WGMs) with effective mode volumes below  $8 \times (\lambda/n)^3$  and quality factors exceeding  $7 \times 10^4$ , where  $n$  is the refractive index of diamond and  $\lambda$  is the vacuum wavelength. We observe saturable absorption in these devices for input powers smaller than 100 mW, and isolate its contribution to total cavity loss by measuring the intensity dependence of  $\kappa_a(I)$ . To characterize the nature of the saturable absorption, we perform power-dependent measurements on WGMs between wavelengths

of 940 nm and 1640 nm and observe saturable absorption for modes at wavelengths between 979 nm and 1267 nm. We attribute this previously unobserved effect to the presence of defects in the diamond crystal and discuss its impact on device performance, as well as potential opportunities for dynamic nonlinear photonics [32, 33] and sensing technologies [34].

## 2 Broadband characterization of dense-NV diamond microdisk resonances

To study optical loss in the dense-NV diamond microdisks, we measure their WGM spectrum using a dimpled fibre-taper waveguide [35] positioned adjacent to the cavity, as illustrated in Fig. 1 (c) and described in Refs [6, 36]. Laser light from continuous-wave tunable lasers (Santec TSL-570 and Newport Velocity TLB-6719 and TLB-6721) spanning 940 – 1640 nm was evanescently coupled into the microdisks from the fibre-taper, whose transmission as a function of wavelength was monitored using a photodetector. A typical mode spectrum near 1042 nm—the wavelength often used for absorption based NV magnetometry [37, 38]—is shown in Fig. 1(d), demonstrating  $Q \sim 7 \times 10^4$  and a doublet structure resulting from surface-roughness-induced mode coupling [6]. A transmission spectrum spanning the scan range from 1260 – 1640 nm is shown in Fig. 2 and reveals a series of WGMs (Fig. 2). Additional details of the experimental setup are provided in Appendix B.

To distinguish between fundamental and higher-order WGMs, we simulate the microdisk eigenmodes using the COMSOL Multiphysics finite element solver (FES). Although the cavity was designed with a 4.2  $\mu\text{m}$  diameter, small fabrication-induced variations inevitably introduce dimensional deviations. In particular, the microdisk thickness obtained from the quasi-isotropic undercut fabrication process varies depending on etching conditions. To determine the physical dimensions of the fabricated cavity, we simulate microdisks over a range of diameters and thicknesses and identify the geometry whose free spectral range (FSR) and eigenfrequencies best match those identified using the measured transmission spectra [39]. We find that the simulated and measured fundamental eigenfrequencies exhibit optimal agreement for a diamond microdisk with a 4.15  $\mu\text{m}$  diameter and 800 nm thickness. These experimentally identified TM (TE) modes are highlighted in red (blue) in Fig. 2 (a), and representative cross-sections of the simulated electric field amplitudes for one TM and one TE mode are shown in the inset. The measured fundamental modes exhibit an FSR of approximately 10 THz. The close agreement between measured and simulated eigenfrequencies, shown in Fig. 2 (b), demonstrates the accuracy of the simulated cavity geometry.

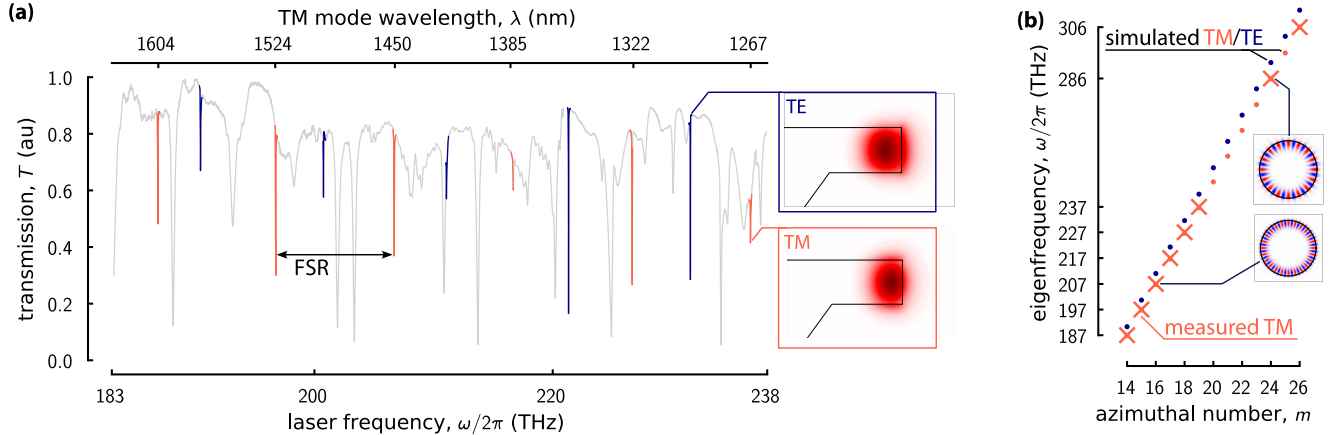


**Figure 2 – Fundamental WGMs in a diamond microdisk.** (a) A wideband transmission spectrum reveals an array of modes, and we highlight the fundamental TM (TE) modes in red (blue). Eigenmodes of the resonator are simulated using a finite element solver, and insets show the simulated TM and TE mode field distributions (azimuthal mode number  $m = 18$ ) inside the microdisk. (b) The simulated eigenfrequencies, marked using 'x' scatter points, align with the measured ones, marked using the dot scatter points. The azimuthal field distribution of two of the modes are shown as insets to (b). Note that the two highest energy TM eigenmode transmission spectra are not shown in (a).

Beyond enabling reliable mode identification, the FES simulations provide the effective mode volume and group index for each WGM, both of which are required to calculate the intracavity optical intensity from experimentally measured parameters. Because these quantities are derived from the simulated cavity geometry, their accuracy depends on the fidelity of the geometric model. The strong agreement between measured and simulated eigenfrequencies indicates that the simulation-derived parameters accurately represent the experimental microdisk. Consequently, uncertainties associated with derived quantities such as the effective mode volume are expected to be significantly smaller than uncertainties associated with other experimental parameters, including the absolute laser power and fibre-taper coupling efficiency. Additional details regarding the eigenmode simulations are provided in Appendix C.

### 3 Observation of saturable absorption in dense-NV diamond

Next, we investigate the power-dependent properties of the fundamental WGMs identified in Fig. 2. We observe that several modes exhibit power-dependent changes in their loss rates and associated transmission lineshapes, which we attribute to the excitation of a saturable absorber within the cavity. To quantify this behaviour, we extract the internal cavity energy loss rate by measuring the fibre-taper transmission spectra across each TM WGM, focusing on TM rather than TE modes due to their greater abundance within the sampled wave-

length range and to avoid any polarization-dependent effects. Near resonance, photons from the fibre-taper (see Fig. 3 (a)) couple into a WGM where they circulate until they are scattered back into the fibre-taper, absorbed by defects, or lost through other mechanisms. By modifying the laser power,  $P$ , input to the fibre-taper, we measure the cavity loss rates over a range of intracavity intensity.

Among the modes studied, only the three modes with the highest frequencies exhibit power-dependent spectral lineshapes. In Fig. 3 (b), we compare the transmission spectra of one of the modes that exhibits strong power dependence (1047 nm) with that of a mode whose transmission spectra is power-independent (1604 nm). The 1047 nm mode possesses a higher intrinsic quality factor and appears as a doublet mode, while the 1604 nm mode possesses a lower quality factor and appears as a singlet. Note that the doublet structure arising from coherent back-scattering between clockwise and counterclockwise propagating WGMs [40] does not directly influence defect absorption (see Appendix A). More importantly, the 1047 nm mode exhibits clear power-dependent changes. The transmission contrast increases with power while linewidth decreases, indicating a reduction in internal cavity loss  $\kappa_a$  and a corresponding increase in  $Q$  with increasing intracavity intensity. In contrast, the absence of comparable power-dependent spectral changes for the 1604 nm mode suggests that the nonlinear loss mechanism responsible for the observed behaviour is strongly wavelength-dependent.

To account for differences in mode properties and better understand the observed nonlinear response, we systematically investigate the intracavity intensity-

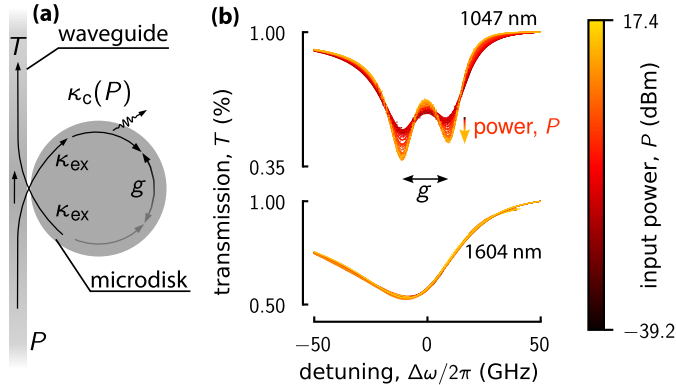


**Figure 3 – Power-dependent laser transmission scans in a microdisk.** (a) Photons coupled into and out of the microdisk at rate  $\kappa_{\text{ex}}$ , and the internal cavity loss is power-dependent,  $\kappa_c(P)$ . (b) By varying the power injected into the WGM cavity, we measure power-dependent transmission spectra for two different modes, each with a different eigenfrequency. The WGM with the higher eigenfrequency (1047 nm) exhibits nonlinear lineshape dependence on  $P$ , whereas the low eigenfrequency mode shows no power dependence. The increase in transmission contrast and reduction in linewidth of the Lorentzian signifies a reduction in loss.

dependent transmission spectra of the eight observed fundamental TM WGMs ranging from 979 nm to 1604 nm. The resulting transmission spectra are fit using a model derived from coupled-mode theory that incorporates coherent back-scattering [40], Fano interference [41], and thermo-optic effects [3, 42] to extract the power-dependent internal cavity loss  $\kappa_c$  (see Appendix A) [3]. The extracted values of  $\kappa_c$  for each mode are plotted in Fig. 4 as a function of the intracavity photon number,  $\mathcal{N}_{\text{cav}}$ , calculated from the power dropped into the cavity mode and the experimentally determined cavity parameters (see Appendix C). Uncertainties in the fitted loss rates are determined from the residuals of the Jacobian matrix obtained during the least-squares fitting procedure and are dominated by uncertainties in the input power,  $P$ , and the fibre coupling efficiency,  $\eta_{\text{fibre}}$ . Additional details regarding the extraction of cavity loss rates are provided in Appendix D.

As shown in the left panel of Fig. 4, significant power-dependent changes in  $\kappa_c$  are observed only for optical modes at 979 nm, 1047 nm, and 1267 nm. For these modes,  $\kappa_c$  decreases nonlinearly with increasing  $\mathcal{N}_{\text{cav}}$  and, in the case of the 1047 nm mode, clear saturation of the loss is observed. For clarity, the right panel of Fig. 4 highlights the evolution of  $\kappa_c$  for the 1047 nm and 1267 nm modes as a function of both the average intracavity intensity,  $\langle I \rangle$ , and  $\mathcal{N}_{\text{cav}}$ , which are related by the mode volume of each WGM (see Section C). We attribute this nonlinearity to the presence of saturable

absorbers in the diamond microdisk. In contrast, modes at wavelengths longer than 1267 nm exhibit no measurable intensity dependence over the investigated input power range.

Applying a two-level saturable absorber model to the observed nonlinearities enables extraction of key characteristics of the defect absorbers. In a cavity, the energy loss rate due to material absorption is proportional to the absorption coefficient,  $\alpha$  [43]:

$$\frac{\kappa_a}{2\pi} = v_g \alpha \approx \frac{c}{n_g} \alpha, \quad (2)$$

where  $v_g$  and  $n_g$  are the group velocity and group index of the mode, respectively, and the approximation holds in the weak dispersion limit [43]. Absorption by an ensemble of two-level systems is proportional to the absorber density,  $M$ , and the frequency-dependent absorption cross-section,  $\sigma_\omega$ , and can saturate at high intensities

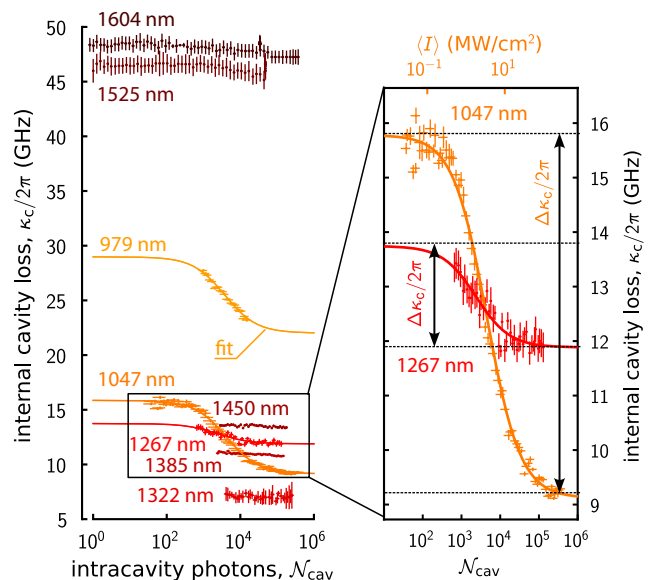


**Figure 4 – Intensity-dependent loss in a microdisk.** Internal cavity loss rate as a function of intracavity photon number for WGMs between 979 nm and 1604 nm. Three WGMs at wavelengths 979 nm, 1047 nm, and 1267 nm exhibit nonlinear dependence of loss rate on optical intensity, which we attribute to a saturable absorber. The right plot highlights the intensity-dependent internal cavity loss rate of the 1047 nm and 1267 nm doublet modes, to which we fit a saturable absorber model to extract the change in internal cavity loss and saturation intensity. In the right figure, the  $\mathcal{N}_{\text{cav}}$  axis pertains to both wavelengths; however, the conversion between  $\mathcal{N}_{\text{cav}}$  and  $\langle I \rangle$  is wavelength-dependent, so the  $\langle I \rangle$  axis pertains only to the 1047 nm mode. The scatter points are the measured data with fit lines corresponding to Eq. (4). See the main text for more details.

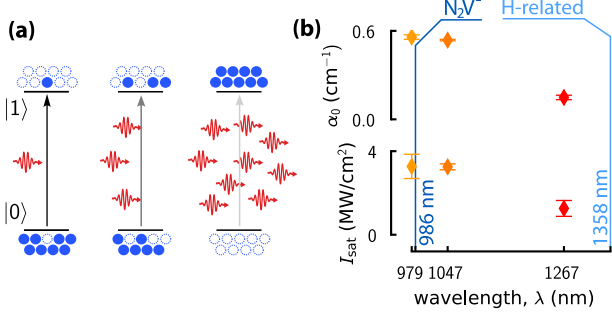


**Figure 5 – Saturable absorption a diamond microdisk.** (a) Saturation of defect absorbers. At low optical intensities (left), most defects are in the ground state. Higher intensities (middle, right) cause the defect population to invert, reducing material absorption loss. (b) Extracted wavelength-dependent linear absorption coefficients and saturation intensities of the saturable absorbers. The zero-phonon lines for the two candidate defects are shown using two vertical blue lines.

due to population inversion (Fig. 5 (a)) [44]:

$$\alpha = \frac{M\sigma\omega}{1 + \frac{\langle I \rangle}{I_{\text{sat}}}}, \quad (3)$$

where  $I_{\text{sat}} = \hbar\omega/\sigma\omega\tau$  is the saturation intensity and  $\tau$  is the lifetime of the excited state. Combining Eqs. (1) to (3) yields an intensity- and frequency-dependent expression for  $\kappa_c$ :

$$\frac{\kappa_c}{2\pi} = \frac{\kappa_i}{2\pi} + \frac{\kappa_p}{2\pi} + \frac{c}{n_g} \frac{\alpha_0}{1 + \frac{\langle I \rangle}{I_{\text{sat}}}}, \quad (4)$$

where  $\alpha_0 = M\sigma\omega$  is the linear absorption coefficient. Equation 4 is used to fit the data shown in Fig. 4, yielding wavelength-dependent absorption coefficients and saturation intensities. These extracted parameters are presented in Fig. 5 (b) and summarized in Tab. 1. Further details on the saturable absorber model can be found in Appendix E.

We primarily attribute the saturable absorption to a hydrogen-based defect [45], although the  $\text{N}_2\text{V}^-$  [46] or other defects may also play a role. A variety of known hydrogen-based defects can be found in diamond [31, 45]; however, neither the density nor the exact composition of the one likely responsible for the observed saturable

**Table 1 –** Extracted linear absorption coefficients and saturation intensities at different wavelengths in diamond.

wavelength, $\lambda$ (nm)	$\alpha_0$ ( $\text{cm}^{-1}$ )	$I_{\text{sat}}$ ( $\text{MW}/\text{cm}^2$ )
979	0.55 (2)	3.3 (6)
1047	0.537 (5)	3.3 (1)
1267	0.15 (2)	1.3 (4)

absorption is known. The defect predominantly occurs in diamond grown using chemical vapour deposition [45, 47] and was recently observed in a study of the same diamond material employed here [19, 38].

The hydrogen-based defect’s zero-phonon line (ZPL) at 1358 nm and broad phonon sideband [38] are consistent with the observed absorption at 979 nm, 1047 nm, and 1267 nm, as well as its absence at wavelengths longer than 1358 nm. Despite it being energetically favourable, saturable absorption of the 1322 nm mode is unexpectedly absent. Several explanations are possible. First, due to several experimental restrictions, the dynamic power range at 1322 nm was restricted and may have been insufficient to observe saturation (see Appendix B). Second, the nonlinearity at this wavelength may be too weak to be distinguished from the measurement uncertainty.

Another defect that could contribute to the saturable absorption is the  $\text{N}_2\text{V}^-$  defect—a nitrogen complex point defect found in diamond [21, 46]. The optically active defect occurs in nitrogen-rich diamond, such as the sample studied here, and has a ZPL near 986 nm with a broad phonon sideband [21]. Although absorption at the 979 nm mode by the  $\text{N}_2\text{V}^-$  defect is energetically favourable, its lifetime ( $\sim 0.3$  ns) and correspondingly narrow ZPL ( $\sim 5$  nm) suggest that it is unlikely to significantly contribute to absorption at longer wavelengths [48]. Therefore, we primarily attribute the observed saturable absorption to the hydrogen-based defect.

#### 4 Effects of loss in diamond photonic cavities

The presence of this absorber impacts a range of applications that are sensitive to optical loss. In particular, these defects are detrimental to the performance of photonic cavities. Our results indicate that the intrinsic  $Q$  of an under-saturated, absorption-limited optical mode with a resonance near 1000 nm cannot exceed  $5 \times 10^4$ . Higher  $Q$  can be achieved at intracavity intensities above saturation, such as those used to measure the cavity shown in Fig. 1 (d). This limitation is expected to be even more severe near the ZPLs of both defects discussed. These effects will primarily impact applications that rely on highly nitrogen-doped diamond, such as NV ensemble based quantum sensors. One particularly affected application is IR absorption-based diamond magnetometry, where changes in external magnetic fields are inferred from absorption of IR (1042 nm) light by the  $\text{NV}^-$  singlet state [38, 49]. Absorption by the  $\text{NV}^-$  singlet state is typically inferred from a change in the transmission of a laser near 1042 nm; however, the saturable absorbers studied here introduce additional absorption loss, thereby limiting the relative change in transmission and corresponding magnetic sensitivity [16, 50]. However, as shown here, saturating the absorption may allow its impact to be

reduced.

Despite these limitations, the presence of a saturable absorber may provide advantages for certain photonic applications. Saturable absorption by solid-state defects has long been exploited for passive control of light–matter interactions, particularly in compact laser systems [33]. In microcavity platforms, an intrinsic saturable absorber can enable passive  $Q$ -switching and mode-locking, producing pulsed or modulated optical output without additional intracavity components or active modulation [32, 51]. Although the linear absorption coefficient found here is smaller than those reported at comparable wavelengths for Cr:YAG ( $\sim 280 \text{ cm}^{-1}$ ) and V:YAG ( $\sim 1.44 \text{ cm}^{-1}$ ) saturable absorbers, diamond-based defect absorbers may nonetheless be suited to similar applications [52, 53]. Because the absorption coefficient scales with defect density (Eq. (3)), diamond samples with higher concentrations of the relevant defects could achieve larger saturable absorption coefficients, increasing their practical utility. Moreover, diamond’s exceptional thermal conductivity and high optical damage threshold [1] suggest that defect-mediated saturable absorption could support high-power or high-repetition-rate pulsed operation in diamond photonic devices.

Beyond laser systems, defect-based saturable absorbers may also enable nonlinear and all-optical signal processing in diamond. In this work, we observe a maximum 42% reduction in loss due to the saturable absorber (Fig. 4), which, after accounting for the external coupling rate, corresponds to an approximately 14% change in transmission contrast (Fig. 3). Although this modulation depth is partially limited by additional sources of cavity loss, improvements in fabrication that reduce background loss could significantly enhance the observable nonlinear response, increasing the utility of these defects for photonic signal processing applications. The intensity-dependent transmission associated with saturable absorption can enable optical switching, optical logic operations [54], and is the subject of intense research within the context of neuromorphic computing [55]. In nanophotonic cavities, where strong field confinement enhances light–matter interactions, even relatively weak absorbers can produce substantial nonlinear responses at relatively low input powers. These properties suggest that diamond microcavities incorporating such defects could serve as compact, integrable nonlinear optical elements for on-chip photonic circuits.

## 5 Conclusion

In this work, we demonstrate and characterize saturable absorption in high- $Q/V$  diamond microdisk cavities fabricated from dense-NV diamond. Using power-dependent measurements of transmission spectra across whispering-

gallery modes spanning 979 nm to 1604 nm, we observe a nonlinear reduction in cavity loss for modes near 979 nm, 1047 nm, and 1267 nm. Using a two-level saturable absorber model, we extract wavelength-dependent absorption coefficients and saturation intensities and identify a hydrogen-based defect as the likely cause of the saturable absorption. The  $\text{N}_2\text{V}^-$  centre is also highlighted as a potential culprit. At 1047 nm, we find that the defects saturate at an intensity of  $I_{\text{sat}} = 3.3 (1) \text{ MW/cm}^2$ , with an absorption coefficient of  $\alpha_0 = 0.537 (5) \text{ cm}^{-1}$ .

These absorbers introduce a material loss mechanism that can impact the performance of diamond nanophotonic devices and is particularly relevant for quantum sensing technologies that rely on dense-NV ensembles. One such application is IR absorption magnetometry. Here, we characterize an optical mode ( $Q > 7 \times 10^4$ ) overlapping with the 1042 nm singlet transition of the negatively charged NV, demonstrating that these microcavities remain promising candidates for IR absorption magnetometry despite the presence of additional defect-mediated loss. Simultaneously, the observed nonlinear response highlights the potential of intrinsic diamond defects as functional elements for nonlinear and all-optical photonic applications, such as  $Q$ -switching, logic, and neuromorphic computing operations. These results provide new insight into defect-mediated optical loss in diamond nanophotonics and suggest strategies to harness defect-induced nonlinearities in future diamond photonic devices.

## Funding

This work was supported by NSERC (Discovery Grant program and Research Tools and Instruments program), Alberta Innovates (Strategic Research Project), and the Canadian Foundation for Innovation. SF acknowledges support from the Swiss National Science Foundation (Project No. P500PT\_206919).

## Acknowledgments

We acknowledge and thank Joe Itoi and Vinaya K. Kavatmane for helpful discussions.

## Appendix

### A Coupled mode theory

To extract the defect-induced loss rate from the cavity transmission scans, we use coupled mode theory to model the cavity dynamics. Specifically, coupled mode or input-output theory gives us an equation to describe the dynamics of the field amplitudes inside the cavity [56].

For a given azimuthal number,  $m$ , an ideal WGM resonator supports identical degenerate modes—one travelling clock-wise (CW) and the other travelling counter-clock-wise (CCW), as shown in Fig. 6 a. The waveguide (in our case, a single-mode fibre-taper) carries an input field  $\hat{s}$ , which couples to the clock-wise cavity mode  $\hat{a}_{\text{cw}}$  with energy coupling rate  $\kappa_{\text{ex}}$ , which then couples back out into the fibre. The amplitude of the CW cavity mode depends not only on the rate of external coupling, but also on internal cavity loss rates. Fabrication imperfections in the cavity and surface scattering introduce intrinsic loss ( $\kappa_{\text{i}}$ ), the presence of the fibre-taper introduces parasitic loss from coupling to high-order fibre modes or radiation modes ( $\kappa_{\text{p}}$ ), and the presence of atomic defects introduces absorption losses ( $\kappa_{\text{a}}$ ). The total cavity energy loss rate for the CW mode can then be written as [56]

$$\kappa_{\text{c}} \equiv \kappa_{\text{ex}} + \kappa_{\text{i}} + \kappa_{\text{p}} + \kappa_{\text{a}}. \quad (5)$$

It is typically a good approximation to assume that this loss rate identically describes the CCW mode, as sketched in Fig. 6 a. For simplicity's sake we also define an internal cavity loss rate,

$$\kappa_{\text{c}} \equiv \kappa_{\text{i}} + \kappa_{\text{p}} + \kappa_{\text{a}}. \quad (6)$$

The above definitions allow us to write down an equation of motion used to describe the cavity field amplitude [56, 57]

$$\dot{\hat{a}}_{\text{cw}} = \sqrt{\kappa_{\text{ex}}}\hat{s} + i\Delta\omega\hat{a}_{\text{cw}} - \frac{\kappa_{\text{c}}}{2}\hat{a}_{\text{cw}}, \quad (7)$$

where  $\Delta\omega = \omega - \omega_0$  describes the cavity frequency detuning between the laser field at frequency  $\omega$  and the cavity resonance at frequency  $\omega_0$ . The term  $\kappa/2$  denotes the field amplitude decay rate of the cavity, which contains  $N = \langle \hat{a}_{\text{cw}} \rangle^2$  intracavity photons, given an input power of  $P = \hbar\omega\langle \hat{s} \rangle^2$ .

In the steady-state approximation, the amplitude of the cavity field is

$$\langle \hat{a}_{\text{cw}} \rangle = \frac{\sqrt{\kappa_{\text{ex}}}}{\frac{\kappa_{\text{c}}}{2} - i\Delta\omega} \langle \hat{s} \rangle. \quad (8)$$

Input-output theory [56, 58] then lets us write down the transmitted field,  $\langle \hat{t} \rangle = \tau \langle \hat{s} \rangle - \sqrt{\kappa_{\text{e}}}\langle \hat{a}_{\text{cw}} \rangle$ , followed by the

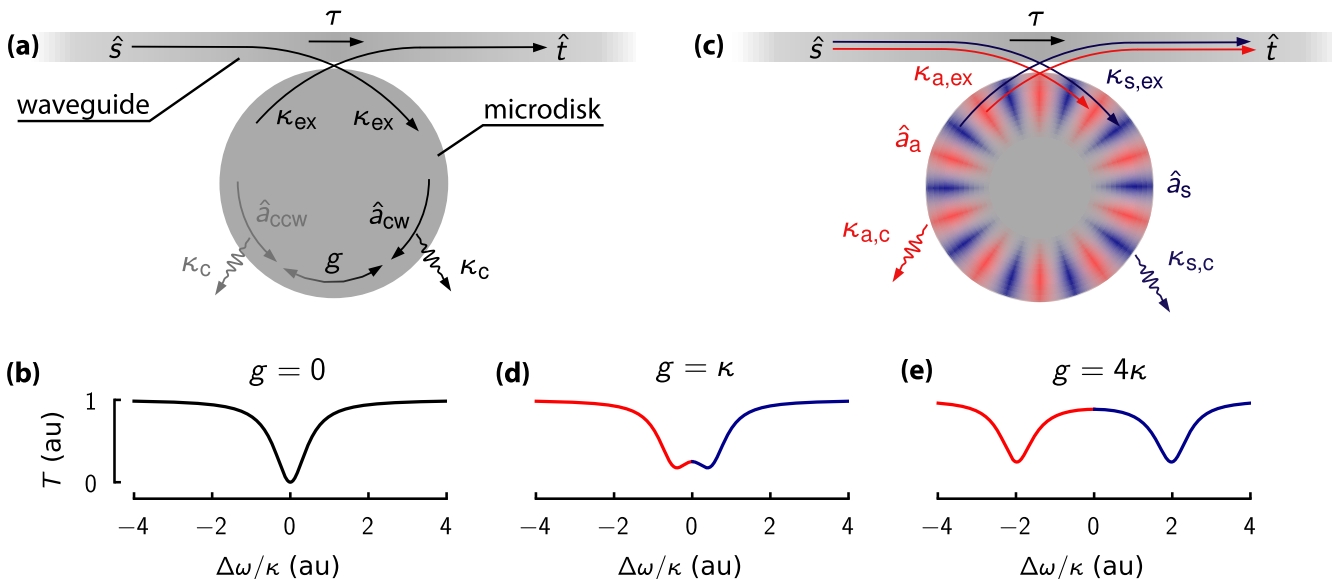


**Figure 6 – Coupled mode theory for a WGM resonator.** (a) An ideal WGM resonator supports identical degenerate modes, one travelling clock-wise (CW) and the other travelling counter-clock-wise (CCW). (b) The transmission spectrum of a coupled waveguide takes the form of a single Lorentzian. In the case that coherent scattering between the two modes is non-negligible ( $g \sim \kappa$ ) the degeneracy is lifted and two standing-wave modes form in the WGM resonator (c): one symmetric (blue) and one antisymmetric (red). The nodes of one mode are located at the anti-nodes of the other. See Section A.1 for more detail. Depending on the strength of the coupling,  $g$ , the transmission spectrum takes the form of a coherent sum of two offset Lorentzians (d, e).

normalized cavity transmission intensity:

$$T \equiv \left| \frac{\langle \hat{t} \rangle}{\langle \hat{s} \rangle} \right|^2 = \left| \tau - \frac{\kappa_{\text{ex}}}{\frac{\kappa_c}{2} - i\Delta\omega} \right|^2. \quad (9)$$

The transmission coefficient  $\tau$  is a complex number and can result in Fano asymmetries in the transmission spectra due to interference between the input and cavity fields [3, 59]. An example transmission spectrum for a critically coupled cavity mode, i.e.  $\kappa_c = \kappa_{\text{ex}}$ , is shown in Fig. 6 (b).

### A.1 Doublet modes

The microdisk supports degenerate WGM modes—one travelling in the clockwise (CW) direction and the other travelling in the counterclockwise (CCW) direction. Surface roughness and imperfections can lead to coherent Rayleigh scattering between the CW and CCW modes [60, 61]. When the back-scattering rate  $g$  is non-negligible, i.e.  $g \sim \kappa$ , the degeneracy between the CW and CCW modes is lifted, resulting in the formation of orthogonal standing-wave modes (Fig. 6 (c)) whose splitting is set by the back-scattering rate (Fig. 6 (d,e)) [40, 62]. By incorporating this back-scattering, the modified equation of motion (Eq. (7)) becomes

$$\dot{\hat{a}}_{\text{cw}} = \left( i\Delta\omega - \frac{\kappa}{2} \right) \hat{a}_{\text{cw}} + i\frac{g}{2}\hat{a}_{\text{ccw}} + \sqrt{\kappa_{\text{ex}}}\hat{s}, \quad (10)$$

$$\dot{\hat{a}}_{\text{ccw}} = \left( i\Delta\omega - \frac{\kappa}{2} \right) \hat{a}_{\text{ccw}} + i\frac{g}{2}\hat{a}_{\text{cw}}. \quad (11)$$

These equations are most easily solved in a new *standing mode* basis [63]

$$\hat{a}_{\text{s}} = \frac{1}{\sqrt{2}} (\hat{a}_{\text{cw}} + \hat{a}_{\text{ccw}}), \quad (12)$$

$$\hat{a}_{\text{a}} = \frac{1}{\sqrt{2}} (\hat{a}_{\text{cw}} - \hat{a}_{\text{ccw}}), \quad (13)$$

where  $\hat{a}_{\text{s}}$  and  $\hat{a}_{\text{a}}$  describe the symmetric and asymmetric standing-wave modes in the WGM resonator. We then use Eqs. (10) to (13) to produce two new equations of motion:

$$\dot{\hat{a}}_{\text{s}} = \left[ i \left( \Delta\omega - \frac{g}{2} \right) - \frac{\kappa}{2} \right] \hat{a}_{\text{s}} + \sqrt{\frac{\kappa_{\text{ex}}}{2}} \hat{s}, \quad (14)$$

$$\dot{\hat{a}}_{\text{a}} = \left[ i \left( \Delta\omega + \frac{g}{2} \right) - \frac{\kappa}{2} \right] \hat{a}_{\text{a}} + \sqrt{\frac{\kappa_{\text{ex}}}{2}} \hat{s}. \quad (15)$$

Heuristically, these equations imply that the resonance frequencies of the two modes are split by  $g = \omega_{\text{a}} - \omega_{\text{s}}$ . They also imply that the input field couples equally well into  $\hat{a}_{\text{s}}$  and  $\hat{a}_{\text{a}}$ ; however, that is not necessarily the case, as the field overlap between the waveguide and  $\hat{a}_{\text{s}}$  or  $\hat{a}_{\text{a}}$  depends on the position of the waveguide

with respect to each mode. Further, the internal loss rates associated with each mode can be different, depending on how the modes interact with the imperfections at the microdisk surface [36]. To generalize Eqs. (14) and (15) to account for these differences, we introduce standing-mode-dependent loss rates ( $\kappa_j = \kappa_{j,\text{ex}} + \kappa_{j,\text{in}}$  for  $j = \text{s, a}$ ), which allow us to express the steady-state field amplitudes as

$$\langle \hat{a}_{\text{s}} \rangle = \frac{\sqrt{\frac{\kappa_{\text{s,ex}}}{2}}}{\frac{\kappa_{\text{s}}}{2} - i \left( \Delta\omega - \frac{g}{2} \right)} \langle \hat{s} \rangle, \quad (16)$$

$$\langle \hat{a}_{\text{a}} \rangle = \frac{\sqrt{\frac{\kappa_{\text{a,ex}}}{2}}}{\frac{\kappa_{\text{a}}}{2} - i \left( \Delta\omega + \frac{g}{2} \right)} \langle \hat{s} \rangle. \quad (17)$$

The normalized transmission intensity is then

$$T = \left| \tau - \sqrt{\frac{\kappa_{\text{s,ex}}}{2}} \frac{\langle \hat{a}_{\text{s}} \rangle}{\langle \hat{s} \rangle} - \sqrt{\frac{\kappa_{\text{a,ex}}}{2}} \frac{\langle \hat{a}_{\text{a}} \rangle}{\langle \hat{s} \rangle} \right|^2 \quad (18)$$

$$= \left| \tau - \frac{\kappa_{\text{s,ex}}}{2} \frac{1}{\frac{\kappa_{\text{s}}}{2} - i \left( \Delta\omega - \frac{g}{2} \right)} - \frac{\kappa_{\text{a,ex}}}{2} \frac{1}{\frac{\kappa_{\text{a}}}{2} - i \left( \Delta\omega + \frac{g}{2} \right)} \right|^2. \quad (19)$$

### A.2 Thermo-optic effects

Populating the optical cavity with large photon numbers causes heating, as dictated by thermo-optic effects [42]. Heating leads to thermal expansion (i.e. the cavity gets larger), which red-shifts the modes. In addition, heating modifies the refractive index via the thermo-optic effect. This effect can be modelled by making the cavity detuning parameter,  $\Delta\omega$ , intracavity-field-dependent [3]. Specifically, replacing  $\Delta\omega \rightarrow \Delta\omega - c_{\text{T}}\langle \hat{a} \rangle^2$ , Eqs. (16) and (17) become

$$\langle \hat{a}_j \rangle = \frac{\sqrt{\frac{\kappa_{\text{ex},j}}{2}}}{\frac{\kappa_j}{2} - i \left( \Delta\omega \pm \frac{g}{2} - c_{\text{T}}\langle \hat{a}_j \rangle^2 \right)} \langle \hat{s} \rangle \quad (20)$$

for  $j = \text{s, a}$ . Here,  $c_{\text{T}}$  is the thermo-optic coefficient, which depends on the geometry and material composition. Equation 20 is cubic in nature, meaning that there are three cavity field solutions; however, we only consider the real part of the solution that matches the experimental results [3]—generally, this corresponds with the solution that gives the fewest intracavity photons,  $\mathcal{N}_j = \langle \hat{a}_j \rangle^2$ . The normalized intensity transmission (Eq. (19)) becomes

$$T = \left| \tau - \frac{\kappa_{\text{s,ex}}}{2} \frac{1}{\frac{\kappa_{\text{s}}}{2} - i \left( \Delta\omega - \frac{g}{2} - c_{\text{T}}\mathcal{N}_{\text{s}} \right)} - \frac{\kappa_{\text{a,ex}}}{2} \frac{1}{\frac{\kappa_{\text{a}}}{2} - i \left( \Delta\omega + \frac{g}{2} - c_{\text{T}}\mathcal{N}_{\text{a}} \right)} \right|^2. \quad (21)$$

## B Experimental setup

The sample under investigation is a "quantum grade" diamond with dense-NV ( $[NV] = 4.5$  ppm), grown by Element Six (DNV<sup>TM</sup> B14 sample type) using chemical vapour deposition [19]. Diamond microdisks are fabricated from the substrate using a quasi-isotropic reactive ion etch undercut method [4, 6]. The resulting devices support whispering-gallery modes (WGMs), and these same devices have been used to perform fluorescence-based magnetometry [18].

Coherent mode spectroscopy [36] for wavelengths between 940–1640 nm is performed to characterize the microdisk using the experimental setup is shown schematically in Fig. 7 (a). To span the wavelength range, we use five different lasers including two Newport lasers (TLB-6719, 940 – 985 nm and TLB-6721, 1030 – 1070 nm), and three Santec lasers (TSL-570 1260 – 1360 nm, 1357 – 1503 nm, 1480 – 1640 nm). To extend the dynamic intensity range of some of the transmission measurements, we optically amplify the transmitted light of the TLB-6721 (1030 – 1070 nm) and TSL-570 (1480 – 1640 nm) lasers using an yttrium-doped fibre amplifier (Thorlabs YDFA100S) and an erbium-doped fibre amplifier (Pritel LNHP-FA-27-IO-CP), respectively. Prior to cavity insertion, an EXFO FVA-3100 variable attenuator is used to control the input power. Fibre coupling to a diamond microdisk is achieved using a dimpled fibre-taper [35, 36] and coupling is maximized by optimizing polarization with the use of a fibre paddle controller. The cavity output couples back into the dimpled fibre-taper and is further attenuated by a second EXFO FVA-3100 in order to maintain approximately constant incident power

on the New Focus nanosecond IR photodetector (Model 1621 or 1623 as required by probe wavelengths being measured).

Several extracted parameters, including the intracavity photon number (Eq. (30)), depend on the transmission efficiency of the fibre,  $\eta_{\text{fibre}}$  at different wavelengths. Therefore, for each laser we directly measure  $\eta_{\text{fibre}}$ , as shown in Fig. 7 (b).

## C Cavity parameters and eigenmode simulations

Studying the intensity- and wavelength-dependence of absorption by defects necessitates knowledge of the spatial distribution of the optical modes. To do so, we simulate the optical cavity mode using the COMSOL Multiphysics finite element solver, adjusting the radius and thickness of the simulated microdisk so that the resulting eigenfrequencies of the simulated fundamental cavity modes matched the measured ones [39]. This approach gives us a better estimate of the cavity geometry. Specifically, the best fit corresponds to a microdisk diameter of  $d_{\text{disk}} = 4.15$   $\mu\text{m}$  and a thickness of  $t_{\text{disk}} = 800$   $\mu\text{m}$ . Note that these simulations account for material dispersion, assumed to be the same as bulk diamond [64]. Four of the simulated electric field mode profiles are shown in Fig. 8 (a)—specifically, we plot the TM and TE fundamental modes for azimuthal numbers  $m = 16, 24$ . The figure highlights how higher  $m$ -number modes are more confined within the diamond resonator and have smaller effective mode volumes than smaller  $m$ -number modes, as demonstrated by the *mode size* annotation. It also highlights that the TM modes are more confined towards the outside of the disk than their TE-mode counterparts.

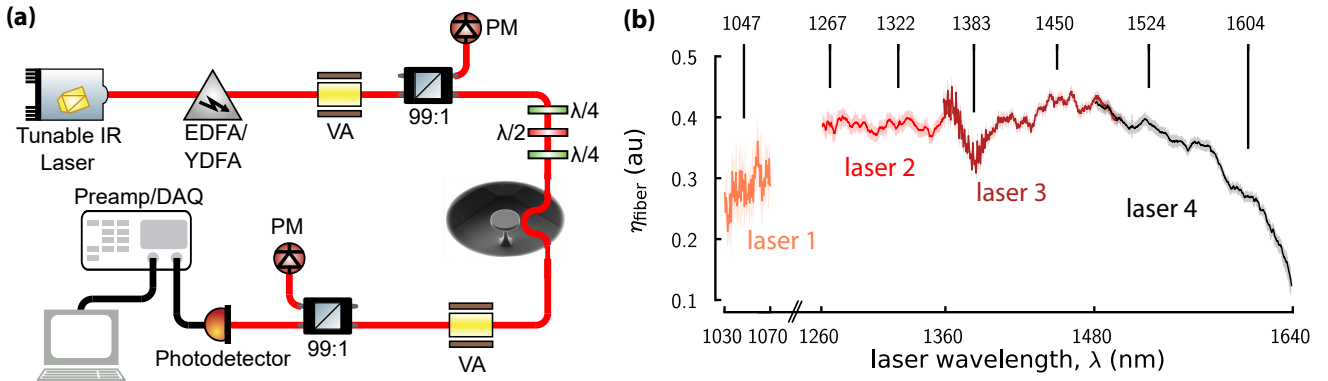


**Figure 7 – Experimental setup and spectral fibre transmission efficiency.** (a) The experiment uses a range of different tunable IR lasers, whose power is controlled using fibre amplifiers (EDFA/YDFA) and variable attenuators (VA). The transmitted laser light is measured using a power meter (PM) before being injected into a microdisk using a dimpled fibre-taper. The transmission is monitored on a photodetector. See the main text for more detail. (b) The bottom axis shows the combined wavelength range of four of the lasers, and the top axis shows the wavelength of each TM mode investigated in this manuscript. Each lineplot shows an averaged transmission spectrum, whereas the shaded region around each lineplot shows the range of each measurement or the effective uncertainty. The transmission scan of the TLB-6719 (940-985 nm) laser is not shown.

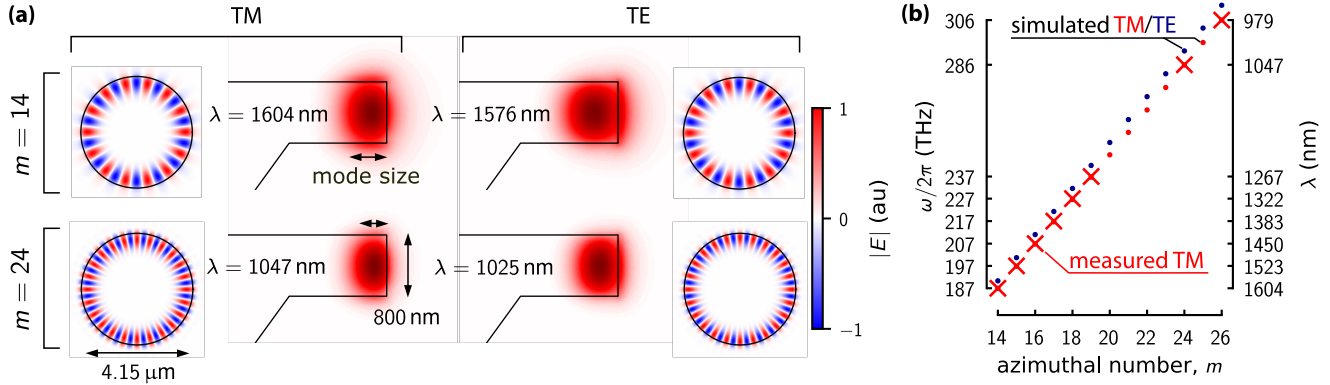


**Figure 8 – Eigenmode simulations.** (a) Spatial field profiles of the diamond microdisk WGMs. The electric field profile of four modes—two TM modes and two TE-modes—is shown from two profiles: from the top, and from a cross-section. (b) Comparison of the eigenvalues of the simulated (dots) and measured (crosses) optical modes. The measured TM modes align very well with the simulated TM modes.

In the following sub-sections we elucidate the calculation of various cavity parameters obtained from simulations. These cavity parameters are used in concert with the measurement-inferred intracavity photon number to deduce the intracavity optical intensity.

### C.1 Average cavity intensity

When considering a nonlinear optical absorption process within a nanophotonic device, it is often desirable to spatially average the local strength of the process over the cavity mode energy density distribution and, in this way, derive an effective mode volume relating intracavity energy to absorption rate [42]. In the case of saturable absorption, this approach is complicated by the non-polynomial scaling of absorption with intensity. We instead approximate the average intensity following the process described below.

The time-averaged intensity of an optical field with energy density  $u(\mathbf{r})$  at position  $\mathbf{r}$  is given by

$$I(\mathbf{r}) = v_g u(\mathbf{r}), \quad (22)$$

where,  $v_g = c/n_g$  is the group velocity,  $c$  is the speed of light in vacuum, and  $n_g$  is the group index. In this work we study single-photon absorption processes, for which the average intensity inside the diamond is the relevant quantity. Assuming that the radial field profile of the mode can be approximated by a Gaussian and that most of the optical field is confined within the diamond absorbing material, we compute a power-weighted average intensity:

$$\langle I \rangle = \frac{\int I^2(\mathbf{r}) dA}{\int I(\mathbf{r}) dA} \quad (23)$$

$$= \frac{1}{2} \max[I(\mathbf{r})]. \quad (24)$$

To justify this approximation we evaluate the confinement factor  $\Gamma_0$ , which gives the fraction of the total electromagnetic energy contained inside the diamond [65]:

$$\Gamma_0 = \frac{\int_{\text{diamond}} u(\mathbf{r}) d^3\mathbf{r}}{\int u(\mathbf{r}) d^3\mathbf{r}}. \quad (25)$$

This confinement factor should be near-unity for the assumption to be valid. To facilitate the calculation of Eq. (24), we define two additional quantities: the effective mode volume  $V_{\text{eff}}$  and the intracavity photon number  $\mathcal{N}_{\text{cav}}$ :

$$V_{\text{eff}} = \frac{\int u(\mathbf{r}) d^3\mathbf{r}}{\max[u(\mathbf{r})]}, \quad (26)$$

$$\mathcal{N}_{\text{cav}} = \frac{1}{\hbar\omega} \int u(\mathbf{r}) d^3\mathbf{r}. \quad (27)$$

The effective mode volume is often expressed in terms of the cavity wavelength  $\lambda$ , yielding a dimensionless mode volume

$$V_0 = V_{\text{eff}} \left( \frac{\lambda}{n_{\text{eff}}} \right)^{-3}, \quad (28)$$

where  $n_{\text{eff}}$  is the effective refractive index of the cavity mode (see Section C.2).

Combining Eqs. (24), (26) and (27) yields

$$\langle I \rangle = \frac{c\mathcal{N}_{\text{cav}}\hbar\omega}{2n_g V_{\text{eff}}}. \quad (29)$$

The validity of Eq. (29) can be assessed by evaluating  $\Gamma_0$  using Eq. (25) together with mode simulations. To evaluate Eq. (29), several parameters must be determined. Both  $n_g$  (see Section C.2) and  $V_{\text{eff}}$  can be extracted from

numerical simulations, while  $\mathcal{N}_{\text{cav}}$  can be calculated from the experimental parameters using

$$\mathcal{N}_{\text{cav}} = \frac{P\sqrt{\eta_{\text{fibre}}}}{\hbar\omega} \left( \frac{\langle \hat{a} \rangle}{\langle \hat{s} \rangle} \right)^2. \quad (30)$$

Here,  $P$  is the optical power injected into the fibre-taper and  $\eta_{\text{fibre}}$  is the transmission efficiency of the fibre-taper at frequency  $\omega$ .

In the case of a cavity doublet, the number of intracavity photons on resonance ( $\Delta\omega = 0$ ) can be calculated for each standing-wave mode:

$$\mathcal{N}_{\text{cav}} = \frac{P\sqrt{\eta_{\text{fibre}}}}{\hbar\omega} \left| \frac{\sqrt{\frac{\kappa_{\text{ex},j}}{2}}}{\frac{\kappa_j}{2} - i\left(\pm\frac{g}{2} - c_{\text{T}}\mathcal{N}_{\text{cav}}\right)} \right|^2, \quad (31)$$

for  $j \in \{\text{s}, \text{a}\}$ . When the thermo-optic shift is non-negligible, Eq. (30) becomes cubic and yields three complex solutions. In such cases we retain the solution whose real part is consistent with the experimentally observed intracavity photon number.

For a cavity singlet, only one travelling-wave mode is populated. To further simplify Eq. (30), we consider a singlet cavity mode ( $g = 0$ ) on resonance ( $\Delta\omega = 0$ ) with no thermo-optic shift ( $c_{\text{T}} = 0$ ). Under these conditions, the intracavity photon number reduces to

$$\mathcal{N}_{\text{cav}}(g = \Delta\omega = 0) = \frac{P\sqrt{\eta_{\text{fibre}}}}{\hbar\omega} \frac{4\kappa_{\text{ex}}}{(\kappa_{\text{ex}} + \kappa_{\text{c}})^2}. \quad (32)$$

Accurate determination of the saturation intensity therefore requires a reliable estimate of  $\eta_{\text{fibre}}$ , which is determined in Appendix B.

## C.2 Group index

Next, we discuss the group index of the resonator, which is used to convert the intracavity photon number into intensity and can be calculated using [66]

$$n_{\text{g}} = c \frac{\partial k_m}{\partial \omega_m}. \quad (33)$$

The group index differs from the effective refractive index, which is approximated by

$$n_{\text{eff}} = \frac{cm}{\omega R_{\text{eff}}}. \quad (34)$$

Here,  $k_m = m/R_{\text{eff}}$  and  $\omega_m$  are the wavenumber and frequency, respectively, of the  $m$ -th mode, with effective radius  $R_{\text{eff}}$ . The effective radius is calculated from the following weighted volume integral:

$$R_{\text{eff}} = \frac{\int r \epsilon(\mathbf{r}) |\mathbf{E}(\mathbf{r})|^2 d^3\mathbf{r}}{\int \epsilon(\mathbf{r}) |\mathbf{E}(\mathbf{r})|^2 d^3\mathbf{r}}, \quad (35)$$

where  $r$  is the axial distance from the centre of the rotationally symmetric microdisk. Generally, both  $m$  and  $R_{\text{eff}}$  are dispersive, so Eq. (33) becomes

$$n_{\text{g}} = \frac{c}{R_{\text{eff}} \frac{\partial \omega}{\partial m}} - \frac{cm}{R_{\text{eff}}^2} \frac{\partial R_{\text{eff}}}{\partial \omega}. \quad (36)$$

All parameters in Eq. (36) can be deduced from simulations of the cavity modes performed using COMSOL Multiphysics.

## C.3 Simulation results

We now simulate the spatial mode profile for all relevant optical modes. The simulated eigenfrequency,  $\omega_{\text{cav}}$ , and azimuthal number,  $m$ , of each fundamental mode are plotted in Fig. 8 (b) alongside their experimentally measured counterparts. The proximity of one of the TM modes to the 1042 nm NV singlet transition and the greater number of TM modes within the sampled wavelength range motivate the study of their properties as opposed to those of the TE-mode counterparts. We must also note that the absence of measured data at TM-mode eigenfrequencies corresponding to  $m \in \{20, 21, 22, 23, 25\}$  is due to the lack of a laser at those wavelengths. By simulating the spatial distribution of each mode, we can ascertain the effective mode volume, refractive index, and group index, allowing us to determine the photon-number-dependent intensities at different wavelengths. We summarize these parameters as predicted by simulation for the TM modes in Tab. 2, calculated using Eqs. (25), (28) and (34) to (36). The near-unity values of the  $\Gamma_0$  in Tab. 2 validate the assumption that most of the field is contained by the diamond, thereby substantiating Eq. (29).

## D Extraction of cavity loss rates

To determine the contribution of defect absorption to the internal loss rate of each fundamental cavity mode, we measure the transmission spectra of each mode at different input powers. The transmission spectra are normalized to the uncoupled fibre-taper transmission spectra (Fig. 7 (b)), and then fitted using Eq. (21). The fits and data for each mode at three different input powers are plotted in Fig. 9. The modes manifest as either singlets or doublets, depending on the rate of back-scattering within the cavity ( $g$ ) compared to the total loss rate ( $\kappa$ ) [40]. Some of the modes also present Fano asymmetries [41] and power-dependent thermo-optic shifts [3, 42]; however, we are primarily interested in how the internal loss rate of each cavity mode changes with input power. The internal loss rate,  $\kappa_{\text{c}}$ , and external coupling rate of each mode at different powers are extracted from each fit and plotted in Fig. 10 (a) and (b), respectively.

**Table 2** – Device parameters for different TM optical modes, calculated from simulation.

$m$	$\lambda_{\text{meas}}$ (nm)	$\lambda_{\text{cav}}$ (nm)	$\omega_{\text{cav}}/2\pi$ (THz)	$V_0$	$\Gamma_0$	$R_{\text{eff}}$ ( $\mu\text{m}$ )	$n_{\text{eff}}$	$n_{\text{g}}$
14	1604	1605	186.8	7.86	0.960	1.84	1.94	2.50
15	1524	1524	196.7	8.64	0.965	1.85	1.97	2.49
16	1450	1451	206.6	9.49	0.969	1.85	1.99	2.47
17	1383	1385	216.5	10.4	0.972	1.86	2.02	2.46
18	1322	1324	226.4	11.4	0.974	1.86	2.03	2.45
19	1267	1269	236.3	12.4	0.977	1.87	2.05	2.44
20	–	1217	246.3	13.4	0.979	1.87	2.07	2.43
21	–	1170	256.3	14.5	0.980	1.88	2.08	2.43
22	–	1126	266.3	15.7	0.982	1.88	2.10	2.42
23	–	1085	276.2	17.0	0.983	1.89	2.11	2.42
24	1047	1047	286.2	18.4	0.984	1.89	2.12	2.41
25	–	1012	296.2	19.8	0.985	1.89	2.13	2.41
26	979	979	306.2	21.3	0.986	1.90	2.14	2.41

For most modes,  $\kappa_c$  is invariant with input power, with the exception of those at 979 nm, 1047 nm, and 1267 nm. In these modes, we observe that internal loss *decreases* with the intracavity photon number, which evidences the presence of a two-level saturable absorber. This change in loss is not due to a change in the external coupling rate,  $\kappa_{\text{ex}}$ , as demonstrated by Fig. 10 (b) . The external coupling rate of each mode remains constant with the number of intracavity photons. Instead, we attribute this to saturable absorption by a point defect found in the diamond.

## E Saturable absorption

In a cavity, the energy loss rate due to linear absorption by defects in the material is proportional to the absorption coefficient,  $\alpha$  [43]:

$$\frac{\kappa_a}{2\pi} = v_g \alpha \approx \frac{c}{n_g} \alpha, \quad (37)$$

where  $v_g$  and  $n_g$  are respectively the group velocity and group index of the mode, and the approximation holds in regions of low dispersion. The group index can be retrieved from simulations, and can be used to convert the measured temporal energy loss rates into a material-dependent absorption coefficient,  $\alpha$ . In turn, the absorption coefficient is proportional to the absorption

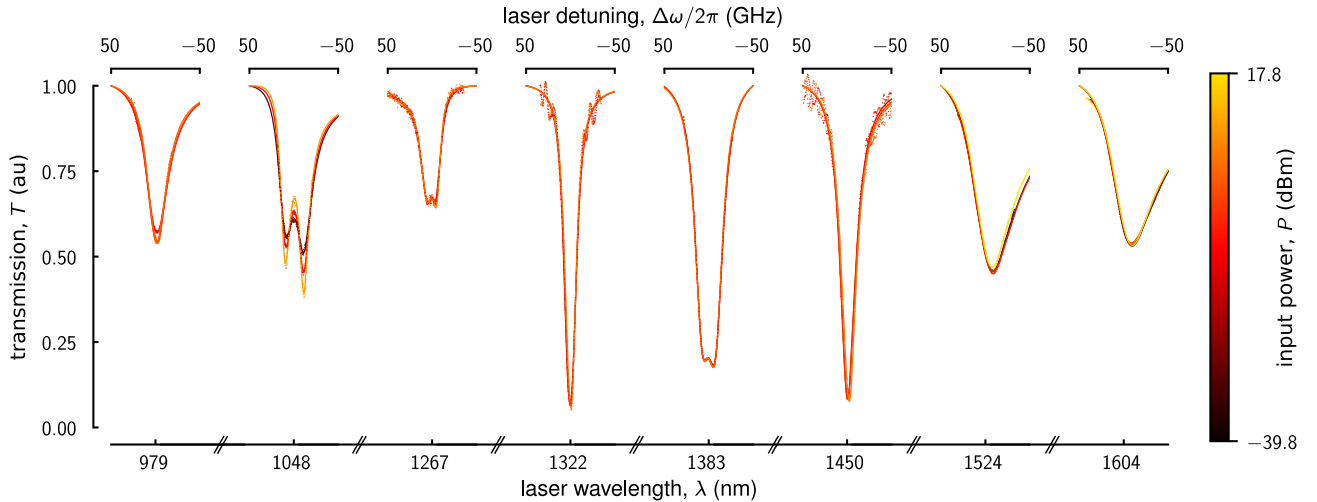


**Figure 9** – Power-dependent cavity transmission spectra. **a.** The transmission spectra of several fundamental TM WGMs measured at different input powers are fit (Eq. (21)) and plotted. Loss parameters and intracavity intensity are extracted from each of these transmission spectra.

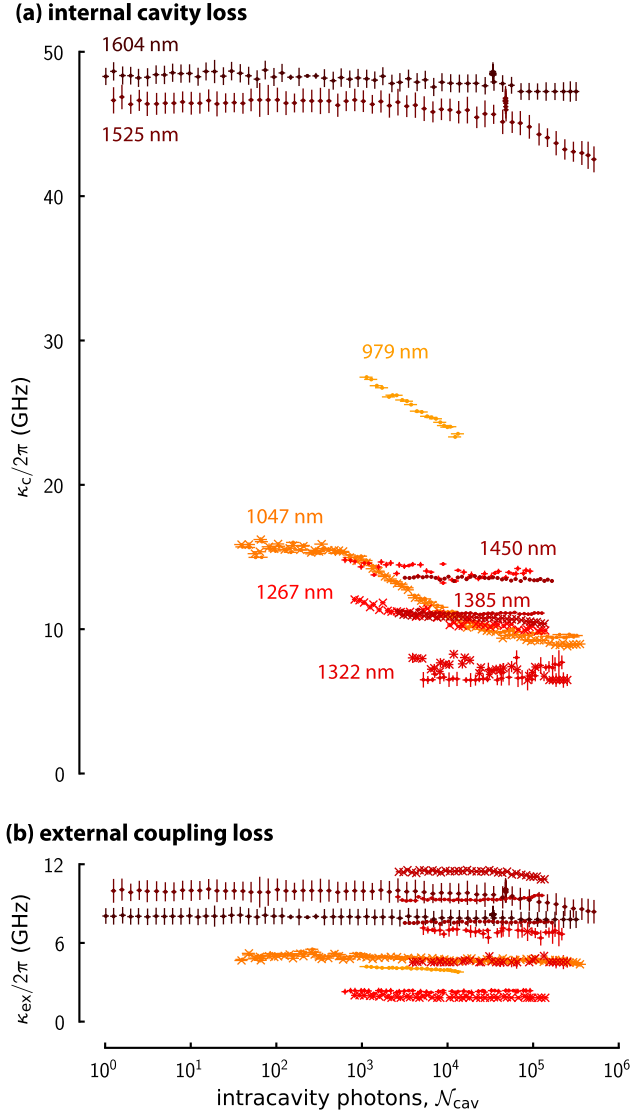


**Figure 10 – Power-dependent cavity loss.** We extract power-dependent cavity- and external-loss rates ( $\kappa_c$  and  $\kappa_{\text{ex}}$ ) from the transmission spectra shown in Fig. 9 and plot them in (a) and (b), respectively. For doublet modes, we plot the cavity loss rates for the symmetric and antisymmetric modes separately and denote them using dot and cross scatter points, respectively. The internal cavity loss rates for most modes remain relatively constant, with the exception of those at 979 nm, 1047 nm, and 1267 nm whereas the external coupling rates remain nearly constant for all modes. The change in  $\kappa_c$  at high powers of the 1525 nm mode correspond with considerable changes in  $\kappa_{\text{ex}}$  signifying either a change in fibre position or an unreliable fit. We omit this data in Fig. 4. Uncertainties in the fitted values were estimated from the residuals of the Jacobian matrix obtained in the least-squares fit, whereas uncertainty in intracavity photon number is primarily due to uncertainty in the measurements of  $P$  and  $\eta_{\text{fibre}}$ .

cross-section at frequency  $\omega$  of a single absorber  $\sigma_\omega$ , the density of absorbers  $M$ , and the intensity-dependent fractional ground state population density of the absorbers,  $m_0$  [44]:

$$\alpha = Mm_0\sigma_\omega = \alpha_0m_0 \quad (38)$$

To determine the intensity-dependent absorption of the defect, we model it as a two-level-system, whose energy levels are separated by  $E = \hbar\omega$  ( $\lambda = 2\pi c/\omega \approx 1358$  nm and  $c$  is the speed of light in vacuum). Off-resonant phonon-assisted absorption of photons with energy greater than  $\hbar\omega$  can incoherently excite the ground state population  $m_0$  to the excited state population  $m_1$ , and is described by the following rate equations [67]:

$$\frac{dm_0}{dt} = -\frac{\sigma_\omega \langle I \rangle}{\hbar\omega} m_0 + \frac{m_1}{\tau} \quad (39)$$

$$\frac{dm_1}{dt} = \frac{\sigma_\omega \langle I \rangle}{\hbar\omega} m_0 - \frac{m_1}{\tau}, \quad (40)$$

where  $\tau$  is the lifetime of the excited state,  $\sigma_\omega$  is the absorption cross-section at frequency  $\omega$ , and  $\langle I \rangle$  is the average intensity inside the diamond cavity at resonance. Given population conservation ( $m_0 + m_1 = 1$ ) in conjunction with Eqs. (39) and (40), the steady-state fractional population density of each state can be expressed as

$$m_0 = \frac{1}{1 + \frac{\langle I \rangle}{I_{\text{sat}}}} \quad (41)$$

$$m_1 = \frac{\frac{\langle I \rangle}{I_{\text{sat}}}}{1 + \frac{\langle I \rangle}{I_{\text{sat}}}}, \quad (42)$$

where  $I_{\text{sat}} = \hbar\omega/\sigma_\omega\tau$  is the saturation intensity of the two-level-system. We then use Eqs. (38) and (41) to express the cavity absorption coefficient in terms of the absorption cross-section, absorber density, and saturation intensity:

$$\alpha = \frac{M\sigma_\omega}{1 + \frac{\langle I \rangle}{I_{\text{sat}}}}. \quad (43)$$

Here,  $\langle I \rangle$  is calculated using Eq. (29) under the assumption that the laser is on resonance with the cavity mode ( $\mathcal{N}_{\text{cav}} = \mathcal{N}_{\text{cav}}(\Delta\omega = 0)$ ). This treatment is an approximation, as it neglects both the dependence of the intracavity intensity—and therefore the absorption—on cavity detuning, as well as the spatial variation of the intensity within the cavity (see Section C.1). Implicitly, Eq. (43) assumes that the intensity is roughly uniform over the absorbing material, which is approximately true in the case of the cavity studied here. In the limits of strong under-saturation and strong over-saturation, this approximation is well justified because the absorption

loss rate is effectively independent of intensity. Consequently, the simplifications used in the model do not significantly affect the extracted linear absorption coefficient,  $\alpha_0$ . However, they may introduce additional uncertainty in the extracted saturation intensity. This is not accounted for in the numerical uncertainty of the saturation intensity values presented in Tab. 1.

Combining Eqs. (6), (37) and (38), we get

$$\frac{\kappa_c}{2\pi} = \frac{\kappa_i}{2\pi} + \frac{\kappa_p}{2\pi} + \frac{c}{n_g} \frac{M\sigma_\omega}{1 + \frac{\langle I \rangle}{I_{\text{sat}}}}. \quad (44)$$

To extract values for the saturation intensity and absorption parameters, this expression can be fit to  $\kappa_c(\langle I \rangle)$  extracted from experimental measurements, as shown in Fig. 4.

## References

1. Shandilya, P.K., Flågan, S., Carvalho, N.C., Zohari, E., Kavatamane, V.K., Losby, J.E., Barclay, P.E.: Diamond Integrated Quantum Nanophotonics: Spins, Photons and Phonons. *Journal of Lightwave Technology* **40**(23), 7538–7571 (2022)
2. Shandilya, P.K., Kavatamane, V.K., Flågan, S., Lake, D.P., Sukachev, D., Barclay, P.E.: Nonlinear optical pumping to a diamond NV center dark state. arXiv:2411.10638 (2024)
3. Itoi, J., Zohari, E., Sorensen, N.J., El-Sayed, W., Losby, J.E., Luiz, G.O., Flågan, S., Barclay, P.E.: Non-volatile photorefractive tuning and green light generation in a diamond cavity. arXiv:2507.19583 (2025)
4. Khanaliloo, B., Mitchell, M., Hryciw, A.C., Barclay, P.E.: High-Q/V monolithic diamond microdisks fabricated with quasi-isotropic etching. *Nano Letters* **15**(8), 5131–5136 (2015)
5. Castelletto, S., Rosa, L., Blackledge, J., Abri, M.Z.A., Boretti, A.: Advances in diamond nanofabrication for ultrasensitive devices. *Microsystems and Nanoengineering* **3**, 17061 (2017)
6. Mitchell, M., Lake, D.P., Barclay, P.E.: Realizing  $Q > 300\,000$  in diamond microdisks for optomechanics via etch optimization. *APL Photonics* **4**(1), 016101 (2019)
7. Kuruma, K., Pingault, B., Chia, C., Haas, M., Joe, G.D., Assumpcao, D.R., Ding, S.W., Jin, C., Xin, C.J., Yeh, M., Sinclair, N., Lončar, M.: Controlling interactions between high-frequency phonons and single quantum systems using phononic crystals. *Nature Physics* **21**(1), 77–82 (2025)
8. Hausmann, B.J.M., Bulu, I., Venkataraman, V., Deotare, P., Lončar, M.: Diamond nonlinear photonics. *Nature Photonics* **8**(5), 369–374 (2014)
9. Latawiec, P., Venkataraman, V., Burek, M.J., Hausmann, B.J.M., Bulu, I., Lončar, M.: On-chip diamond Raman laser. *Optica* **2**(11), 924 (2015)
10. Flågan, S., Itoi, J., Shandilya, P.K., Kavatamane, V.K., Mitchell, M., Lake, D.P., Barclay, P.E.: Optical switching of  $\chi^{(2)}$  in diamond photonics. *Physical Review Letters* **135**, 233801 (2025)
11. Janitz, E., Bhaskar, M.K., Childress, L.: Cavity quantum electrodynamics with color centers in diamond. *Optica* **7**(10), 1232–1252 (2020)
12. Bhaskar, M.K., Riedinger, R., Machielse, B., Levonian, D.S., Nguyen, C.T., Knall, E.N., Park, H., Englund, D., Lončar, M., Sukachev, D.D., Lukin, M.D.: Experimental demonstration of memory-enhanced quantum communication. *Nature* **580**(7801), 60–64 (2020)
13. Beukers, H.K.C., Pasini, M., Choi, H., Englund, D., Hanson, R., Borregaard, J.: Remote-Entanglement Protocols for Stationary Qubits with Photonic Interfaces. *PRX Quantum* **5**(1), 010202 (2024)
14. Burek, M.J., Cohen, J.D., Meenehan, S.M., El-Sawah, N., Chia, C., Ruelle, T., Meesala, S., Rochman, J., Atikian, H.A., Markham, M., Twitche, D.J., Lukin, M.D., Painter, O., Lončar, M., Paulson, J.A.: Diamond optomechanical crystals. *Optica* **3**, 1404–1411 (2016)
15. Shandilya, P.K., Lake, D.P., Mitchell, M.J., Sukachev, D.D., Barclay, P.E.: Optomechanical interface between telecom photons and spin quantum memory. *Nature Physics* **17**(12), 1420–1425 (2021)
16. Jensen, K., Leefer, N., Jarmola, A., Dumeige, Y., Acosta, V.M., Kehayias, P., Patton, B., Budker, D.: Cavity-enhanced room-temperature magnetometry using absorption by nitrogen-vacancy centers in diamond. *Physical Review Letters* **112**, 160802 (2014)
17. Flågan, S., Maletinsky, P., Warburton, R.J., Riedel, D.: Microcavity platform for widely tunable optical double resonance. *Optica* **9**(10), 1197 (2022)
18. Sorensen, N.J., Zohari, E., Wildeman, J.S., Flågan, S., Kavatamane, V.K., Barclay, P.E.: Nanophotonic magnetometry in a spin-dense diamond cavity. arXiv:2511.19831 (2025)
19. Element Six: DNV™ B1 and DNV™ B14. Technical report, Element Six (2021)
20. Aharonovich, I., Castelletto, S., Simpson, D.A., Su, C.H., Greentree, A.D., Prawer, S.: Diamond-based single-photon emitters. *Reports on Progress in Physics* **74**(7) (2011)
21. Ashfold, M.N.R., Goss, J.P., Green, B.L., May, P.W., Newton, M.E., Peaker, C.V.: Nitrogen in diamond. *Chemical Reviews* **120**, 5745–5794 (2020)
22. Czelej, K., Zemła, M.R., Śpiewak, P., Kurzydłowski, K.J.: Quantum behavior of hydrogen-vacancy complexes in diamond. *Physical Review B* **98**, 235111 (2018)
23. Rose, B.C., Huang, D., Zhang, Z.H., Stevenson, P., Tyryshkin, A.M., Sangtawesin, S., Srinivasan, S., Loudin, L., Markham, M.L., Edmonds, A.M., Twitche, D.J., Lyon, S.A., Leon, N.P.D.: Observation of an environmentally insensitive solid-state spin defect in diamond. *Science* **361**, 60–63 (2018)
24. Bradac, C., Gao, W., Forneris, J., Trusheim, M.E., Aharonovich, I.: Quantum nanophotonics with group IV defects in diamond. *Nature Communications* **10**(1), 5625 (2019)
25. Togan, E., Chu, Y., Trifonov, A.S., Jiang, L., Maze, J., Childress, L., Dutt, M.V.G., Sørensen, A.S., Hemmer, P.R., Zibrov, A.S., Lukin, M.D.: Quantum entanglement between an optical photon and a solid-state spin qubit. *Nature* **466**(7307), 730–734 (2010)
26. Knaut, C.M., Suleymanzade, A., Wei, Y.C., Assumpcao, D.R., Stas, P.J., Huan, Y.Q., Machielse, B., Knall, E.N., Sutula, M., Baranes, G., Sinclair, N., De-Eknamkul, C., Levonian, D.S., Bhaskar, M.K., Park, H., Lončar, M., Lukin, M.D.: Entanglement of nanophotonic quantum memory nodes in a telecom network. *Nature* **629**(8012), 573–578 (2024)
27. Stolck, A.J., Enden, K.L., Slater, M.-C., Raa-Derckx, I., Botma, P., Rantwijk, J., Biemond, J.J.B., Hagen, R.A.J., Herfst, R.W., Koek, W.D., Meskers, A.J.H., Vollmer, R., Zwet, E.J., Markham, M., Edmonds, A.M., Geus, J.F., Elsen, F., Jungbluth, B., Haefner, C., Tresp, C., Stuhler, J., Ritter, S., Hanson, R.: Metropolitan-scale heralded entanglement of solid-state qubits. *Science Advances* **10**(44), 6442 (2024)
28. Rondin, L., Tetienne, J.P., Hingant, T., Roch, J.F., Maletinsky, P., Jacques, V.: Magnetometry with nitrogen-

- vacancy defects in diamond. Reports on Progress in Physics **77**(5) (2014)
29. Degen, C.L., Reinhard, F., Cappellaro, P.: Quantum sensing. *Reviews of Modern Physics* **89**(3), 035002 (2017)
  30. Wong, K.C., Ng, S.L., Ho, K.O., Shen, Y., Wu, J., Lai, K.T., Leung, M.Y., Leung, W.K., Dasari, D.B.R., Denisenko, A., Wrachtrup, J., Yang, S.: Microscopic study of optically stable coherent color centers in diamond generated by high-temperature annealing. *Physical Review Applied* **18**, 024044 (2022)
  31. Glover, C., Newton, M.E., Martineau, P., Twitchen, D.J., Baker, J.M.: Hydrogen incorporation in diamond: The nitrogen-vacancy-hydrogen complex. *Physical Review Letters* **90**, 185507 (2003)
  32. Dangoisse, D., Glorieux, P., Hennequin, D.: Nonlinear dynamics of a laser containing a modulated saturable absorber. *Physical Review A* **42** (1990)
  33. Paschotta, R.: *Handbook of Solid-State Lasers* vol. 1, 1st edn., pp. 227–255. (2013)
  34. Qu, Y., Cheng, T., Lan, D., Zhang, X., Wang, F.: Silver sulfide nanoparticles as saturable absorber for Q-switching and refractive index sensor. *IEEE Photonics Technology Letters* **34**, 1345–1348 (2022)
  35. Michael, C.P., Borselli, M., Johnson, T.J., Chrystal, C., Painter, O.: An optical fiber-taper probe for wafer-scale microphotonic device characterization. *Optics Express* **15**(8), 4745–4752 (2007)
  36. Masuda, T., Hadden, J.P.E., Lake, D.P., Mitchell, M., Flågan, S., Barclay, P.E.: Fiber-taper collected emission from nv centers in high- $Q/V$  diamond microdisks. *Opt. Express* **32**(5), 8172–8188 (2024)
  37. Acosta, V.M., Bauch, E., Jarmola, A., Zipp, L.J., Ledbetter, M.P., Budker, D.: Broadband magnetometry by infrared-absorption detection of nitrogen-vacancy ensembles in diamond. *Applied Physics Letters* **97**, 174104 (2010)
  38. Tayefeh Younesi, A., Omar, M., Wickenbrock, A., Budker, D., Ulbricht, R.: Towards high-sensitivity magnetometry with nitrogen-vacancy centers in diamond using the singlet infrared absorption. *Physical Review Applied* **23**, 054019 (2025)
  39. Behjat, P., Parsa, P., Carvalho, N.C., Shandilya, P.K., Barclay, P.E.: Kerr-optomechanical spectroscopy of multimode diamond resonators. *ACS Photonics* **10**(11), 4014–4021 (2023)
  40. Borselli, M., Johnson, T.J., Painter, O.: Beyond the Rayleigh scattering limit in high- $Q$  silicon microdisks: theory and experiment. *Optics Express* **13**, 1515–1530 (2005)
  41. Suh, W., Joannopoulos, J.D., Fan, S.: Temporal coupled-mode theory for the Fano resonance in optical resonators. *Journal of the Optical Society of America A* **20**, 569–572 (2003)
  42. Barclay, P.E., Srinivasan, K., Painter, O.: Nonlinear response of silicon photonic crystal microresonators excited via an integrated waveguide and fiber taper. *Optics Express* **13**(3), 801–820 (2005)
  43. Saleh, B., Teich, M.: *Fundamentals of Photonics* vol. 1, 3rd edn., pp. 201–204. (2019)
  44. Boyd, R.W.: *Nonlinear Optics*, Third Edition, pp. 168–169. (2008)
  45. Fuchs, F., Wild, C., Schwarz, K., Müller-Sebert, W., Koidl, P.: Hydrogen induced vibrational and electronic transitions in chemical vapor deposited diamond, identified by isotopic substitution. *Applied Physics Letters* **66**(2), 177–179 (1995)
  46. Talik, W., Mrózek, M., Wojciechowski, A.M., Dzierżęga, K.: Saturable absorption in NV-doped diamond studied by femtosecond Z-scan. arXiv:2601.12421 (2026)
  47. Inyushkin, A.V., Taldenkov, A.N., Ralchenko, V.G., Shu, G., Dai, B., Bolshakov, A.P., Khomich, A.A., Ashkinazi, E.E., Boldyrev, K.N., Khomich, A.V., Han, J., Konov, V.I., Zhu, J.: Thermal conductivity of pink CVD diamond: Influence of nitrogen-related centers. *Journal of Applied Physics* **133**, 25102 (2023)
  48. Johnson, B.C., Vries, M.O., Healey, A.J., Capelli, M., Manian, A., Thalassinos, G., Abraham, A.N., Hapuarachchi, H., Luo, T., Mochalin, V., Jeske, J., Cole, J.H., Russo, S., Gibson, B.C., Stacey, A., Reineck, P.: The nitrogen-vacancy-nitrogen color center: A ubiquitous visible and near-infrared-II quantum emitter in nitrogen-doped diamond. *ACS Nano* **19**, 19046–19056 (2024)
  49. Marini, U., Marconi, B., Caprini, L., Puglisi, A., Stroeks, M.E., Helsen, J., Terhal, B.M., Rogers, L.J., Armstrong, S., Sellars, M.J., Manson, N.B.: Infrared emission of the NV centre in diamond: Zeeman and uniaxial stress studies. *New Journal of Physics* **10**, 103024 (2008)
  50. Zadeh-Haghighi, H., Golami, O., Kavatamane, V.K., Barclay, P.E., Simon, C.: Master-equation-based model for infrared-based magnetometry with nitrogen-vacancy-centers-in-diamond cavities: A path to subpicotesla sensitivity at submillimeter scales. *Physical Review Applied* **22**, 064015 (2024)
  51. Morris, J.A., Pollock, C.R.: Passive Q switching of a diode-pumped Nd:YAG laser with a saturable absorber. *Optics Letters* **15**(8), 440–442 (1990)
  52. Dong, J., Deng, P., Liu, Y., Zhang, Y., Xu, J., Chen, W., Xie, X.: Passively Q-switched Yb:YAG laser with Cr<sup>4+</sup>:YAG as the saturable absorber. *Appl. Opt.* **40**(24), 4303–4307 (2001)
  53. Liu, C., Zhao, S., Li, G., Yang, K., Li, D., Li, T., Qiao, W., Feng, T., Chen, X., Xu, X., Zheng, L., Xu, J.: Experimental and theoretical study of a passively Q-switched Nd:LuAG laser at 1.3 $\mu$ m with a V<sup>3+</sup>:YAG saturable absorber. *Journal of the Optical Society of America B* **32**(5), 1001–1006 (2015)
  54. Porzi, C., Guina, M., Bogoni, A., Potl, L.: All-optical nand/nor logic gates based on semiconductor saturable absorber etalons. *IEEE Journal of Selected Topics in Quantum Electronics* **14**(3), 927–937 (2008)
  55. Farnakidis, N., Dong, B., Bhaskaran, H.: Integrated photonic neuromorphic computing: opportunities and challenges. *Nature Reviews Electrical Engineering* **1**(6), 358–373 (2024)
  56. Haus, H.A.: *Waves and Fields in Optoelectronics*, p. 402. (1984)
  57. Barclay, P.E., Santori, C., Fu, K.-M., Beausoleil, R.G., Painter, O.: Coherent interference effects in a nano-assembled diamond NV center cavity-QED system. *Optics Express* **17**(10), 8081 (2009)
  58. Clerk, A.A., Devoret, M.H., Girvin, S.M., Marquardt, F., Schoelkopf, R.J.: Introduction to quantum noise, measurement, and amplification. *Reviews of Modern Physics* **82**(2), 1155–1208 (2010)
  59. Fan, S., Suh, W., Joannopoulos, J.D.: Temporal coupled-mode theory for the Fano resonance in optical resonators. *Journal of the Optical Society of America A* **20**(3), 569 (2003)
  60. Gorodetsky, M.L., Pryamikov, A.D., Ilchenko, V.S.: Rayleigh scattering in high- $Q$  microspheres. *Journal of the Optical Society of America B* **17**(6), 1051 (2000)
  61. Lake, D.P., Mitchell, M., Jayakumar, H., Santos, L.F., Curic, D., Barclay, P.E.: Efficient telecom to visible wavelength conversion in doubly resonant gallium phosphide microdisks. *Applied Physics Letters* **108**(3), 031109 (2016)
  62. Borselli, M., Srinivasan, K., Barclay, P.E., Painter, O.: Rayleigh scattering, mode coupling, and optical loss in silicon microdisks. *Applied Physics Letters* **85**(17), 3693–3695 (2004)
  63. Borselli, M.: High- $Q$  microresonators as lasing elements for sil-

- icon photonics. PhD thesis, California Institute of Technology (2006)
64. Phillip, H.R., Taft, E.A.: Kramers-Kronig analysis of reflectance data for diamond. *Physical Review* **136**, 1445–1448 (1964)
  65. Barclay, P.E.: Fiber-coupled nanophotonic devices for nonlinear optics and cavity QED. PhD thesis, California Institute of Technology (2007)
  66. Yariv, A., Yeh, P.: *Photonics: Optical Electronics in Modern Communications*, 6th edn., pp. 14–15. (2007)
  67. Srinivasa Rao, A.: Saturation effects in nonlinear absorption, refraction, and frequency conversion: a review. *Optik* **267**, 169638 (2022)